Variable depths of magma genesis in Eastern Asia inferred from teleseismic P wave attenuation

Liu Hanlin[a,b,c,*], Joseph S. Byrnes[c], Maximiliano Bezada[c], Wu Qingju[a,*], Pei Shunping[b], He Jing[d]

[a] Key laboratory of Seismic Observation and Geophysical Imaging, Institute of Geophysics, China Earthquake Administration, Beijing, 100081, China

[b] State Key Laboratory of Tibetan Plateau Earth System Science (LATPES), Institute of Tibetan Plateau Research, Chinese Academy of Sciences (CAS), Beijing, 100101, China

[c] Department of Earth Sciences, University of Minnesota, Twin Cities, United States of America

[d] National Institute of Natural Hazards, Ministry of Emergency Management of People's Republic of China, Beijing, 100085, China

[*] Corresponding authors

Correspondence to: Liu Hanlin: lhlgeoph@outlook.com; Wu Qingju: wuqj@cea-igp.ac.cn

Abstract: Eastern Asia is a prime location for the study of intracontinental tectono-magmatic activity. For instance, the origin of wide-spread intraplate volcanism has been one of the most debated aspects of East Asian geological activity. Measurements of attenuation of teleseismic phases may provide additional constraints on the source regions of volcanism by sampling the upper mantle. This study uses data from three seismic arrays to constrain lateral variations in teleseismic P-wave attenuation beneath the Central Orogenic Belt and the North China Craton. We invert relative observations of attenuation for a 2-D map of variations in attenuation along with data and model uncertainties by applying a Hierarchical Bayesian method. As expected, low attenuation is observed beneath the Ordos block. High attenuation is observed beneath most of the volcanoes (e.g., the Middle Gobi volcano, the Bus Obo volcano and the Datong volcano) in the study area, and estimated asthenospheric Qp values span from 95 to 200. These values are within the range of globally average asthenosphere. We infer that these volcanoes may tap melt from ambient asthenosphere and occur where the lithosphere is thin, which is consistent with previous petrologic studies. More complex mantle drivers of volcanism are not rejected but are not needed to explain eruptions in this area. In contrast, at the Xilinhot-Abaga volcanic site, the observed low attenuation (as low as beneath the Ordos block) excludes a typical shallow melting column. Fluids from the subducted Pacific plate may initiate the deep melting and would be consistent with petrological constraints.

Key points:

1. The teleseismic P-wave attenuation is obtained in Central Asian Orogenic Belt and North China Craton.

2. Most volcanism in study area may tap melt from ambient asthenosphere and occur where the lithosphere is thin.

3. A thick lithosphere and a deep magma source are inferred beneath the Xilinhot-Abaga volcanic site.

Plain Language Summary: Seismic attenuation provide complementary constraints in contrast to velocity in travel time, as attenuation focuses on energy loss and frequency information of seismic waves when passing through rocks. We present the first teleseismic attenuation map in Central Asian Orogenic Belt and North China Craton based on 829 direct P phases from 38 deep teleseismic events. We find low attenuation beneath the Ordos Block and elevated attenuation beneath most of the volcanic sites in the study region (e.g., the Middle Gobi volcano, the Bus Obo volcano and the Datong volcano), which is consistent with expectations of the sensitivity of attenuation to temperature. Our results suggest that the asthenosphere beneath the study region is as attenuating as global average. we infer most of the volcanism in this portion of Eastern Asia may tap melt from ambient asthenosphere and occur where lithosphere is thin, which is consistent with previous petrologic studies. Counter-intuitive low attenuation is observed beneath the Xilinhot-Abaga volcanic site, which excludes a typical shallow melting column and is consistent with a deep melting magma source. The magma genesis across the study area are consistent with lithospheric thickness as a primary cause of variations in the composition of erupted lavas.

1. Introduction

Much of the geological activity on Earth occurs at plate boundaries in accordance with the theory of plate tectonics. However, magmatism and tectonic deformation can occur far from plate boundaries in continental interiors, (e.g., Molnar and Tapponnier, 1975; Molnar and Deng, 1984; Barry and Kent, 1998; Walker et al., 2007). Eastern Asia is a prime example. Intracontinental volcanism, orogenic uplift, and metasomatism all occurred in Eastern Asia during collision between India and Asia to the southwest, subduction of the Pacific plate to the east, and widespread mantle upwelling (e.g., Molnar et al., 1993; Tapponnier et al., 2001; Schellart and Lister, 2005; Li et al., 2012). The effect of these processes on the already heterogenous continental lithosphere leads to many styles of deformation and magmatism within the continent (Fig. 1), making this area a unique site to explore intraplate activity (e.g., Griffin et al., 1998; Xu, 2001; Deng et al., 2004; Wang et al., 2006; Barry et al., 2007).

Seismic imaging of the Earth's interior can aid our understanding of such processes. The most commonly imaged seismological parameter is seismic velocity, while seismic attenuation may have greater importance when inferring the physical state of the subsurface (Karato, 1993; Goes et al., 2000; Hammond and Humphreys, 2000). Seismic velocity is relatively well characterized across Eastern Asia (e.g., Priestly et al., 2006; Tian et al., 2009; Li and van der Hilst, 2010; Lei, 2012; Li et al., 2013; Tao et al., 2018), while seismic attenuation across the region is poorly understood. Constraints on variation in seismic attenuation can reflect variations in temperature, the presence of fluids, partial melting, composition and grain size (e.g., Dziewonski et al., 1982; Gomer and Okal, 2003; Dalton and Faul, 2010), and so can aid our understanding of volcanism, seismicity, and variations in the strength of the lithosphere. Though several investigations of seismic attenuation have been conducted (e.g., He et al., 2017), the deep attenuation structure beneath Eastern Asia is still unknown, since previous studies used seismic phases (Lg, Sn, Pg, Pn) that are only sensitive to the crust and the uppermost mantle.

In this study, we used combined data recorded by three temporary seismic arrays (Fig. 1), located in Central Mongolia (CM array), Inner Mongolia, China, around the Xilinhot-Abaga (XA, hereafter) volcanic site (NM array), and the Western and Central Blocks of the NCC (OD array), to estimate teleseismic P wave attenuation by applying a time-domain waveform matching method (Adams and Humphreys, 2010; Bezada, 2017; Byrnes et al., 2019). We obtained a 2-D map of relative attenuation structure which shows significant lateral heterogeneity. The attenuation structure we image is closely associated with local tectonic features and deep asthenosphere processes. We find low attenuation beneath the Ordos block and elevated attenuation beneath most volcanic sites, which is consistent with expectations. Counter-intuitively, low attenuation is also found beneath the XA. We discuss the tectonic implications as well as outstanding questions that we suggest as promising areas for future research.

1.1 Regional Tectonic Background

The study area is located at the center of Eastern Asia (Fig. 1), containing South-central

Mongolia and the XA volcanic site in the Central Asian Orogenic Belt (CAOB), and the western and central parts of the North China Craton (NCC) (Fig. 1). The Mongolian plateau is located in the core of the CAOB, one of the largest Paleozoic continental orogens on Earth (Windley et al., 2007). Its high-standing topography (mean elevation of ~1500 m) is perplexing, given that it is far from any plate boundaries. The Hangay Dome, in the west of the study region, reaches ~4000 m, and the Khentii Mountains, within the study region, rise to ~3000 m. Even the Gobi Desert, which is low-standing for the region, sits at an average elevation of ~1000 m (Barry and Kent, 1998; Walker et al., 2007). Two possible and widely accepted models for the significant regional elevation are lithospheric processes due to far-field effects of the India-Asia collision or high asthenospheric temperatures due to an upwelling plume (e.g., Molnar and Tapponnier, 1975; Windley and Allen, 1993; Mordinova et al., 2007; Hunt et al., 2012; Chen et al., 2015a).

Also noteworthy are the abundant, low-volume Cenozoic intraplate volcanoes that have erupted over the past 30 Ma. This is expressed in numerous, small volume, alkali-basalt cones that extend from the Baikal Rift across central Mongolia to north and northeast China (Barry, 2003; Hunt et al., 2012). Examples include the Middle Gobi and Bus Obo magmatic centers on the northwest and northeast of the Gobi Desert, respectively, and the Dariganga Volcanic site on the boundary between China and Mongolia (Fig. 1). The latter is connected to the XA volcanic province in China and represents the largest volcanic province in central and eastern Asia (Fig. 1) (Ho et al., 2008; Barry and Kent, 1998). The XA is located in Inner Mongolia, China, and consists of more than 300 individual volcanoes and a lava plateau that covers over 10,000 km^2 (Wang et al., 2006; Chen et al., 2015b). K-Ar dating suggests volcanic activity in the XA initiated sometime between the middle Miocene and the early Pleistocene, similar to the Dariganga Volcanic site

(Kononova et al., 2002; Ho et al., 2008).

The North China Craton (NCC), one of the oldest Archean cratons in the world (Liu et al., 1992; Lei, 2012), lies south of the CAOB and is bounded on the north by the Late Paleozoic Yinshan-Yanshan Orogenic Belt (Fig. 1). The NCC became stable in the late Paleoproterozoic after the collision of its eastern and western sections, and was reactivated in the late Mesozoic and Cenozoic (e.g., Xu, 2001; Deng et al., 2004; Lei, 2012). The NCC consists of the eastern NCC, the western NCC and the TNCO (Trans-North China Orogen). The eastern NCC lies to the east of our study area and so will not be discussed further. The western NCC is mainly comprised of the Ordos Block, and the Late Paleozoic Yinshan orogen, which separates it from the CAOB to the north. The Ordos Block is a large Mesozoic intra-continental basin that has uplifted continuously since the Cenozoic (Deng and You, 1985). The Ordos Block has a deep lithospheric keel which reaches over 200 km depth (Tian et al., 2009; Lei, 2012), and is considered to be a stable block given the notable absence of recent seismic and magmatic activity within it (Qiu et al., 2005).

The TNCO is an orogen that records the collision between the western and eastern halves of the NCC (Zhao et al., 2005) (Fig. 1). The Shanxi Graben lies within the TNCO and formed during Late Cenozoic extension in North China, where volcanic rocks are widespread and seismic hazard is high (Xu and Ma, 1992; Deng et al., 1999). The Datong volcanic site located at the northern end of Shanxi Graben (Fig. 1) is a typical representative of TNCO volcanism (Ye et al., 1987; Ren et al., 2002).

1.2 Previous Studies

Several seismological experiments have explored the origin of the high topography and the wide-spread Cenozoic intraplate volcanism in the Mongolian plateau, including the PASSCAL (Program for Array Seismic Studies of Continental Lithosphere) arrays deployed around the Baikal Rift, Siberian Craton and central Mongolia (Gao et al., 1994), the MOBAL (Mongolian-Baikal Lithosphere seismological Transect) array (Barruol et al., 2008), and the CM array (China-Mongolia seismic array) , which is used in the present study (He et al., 2016). Imaging based on data from the PASSSCAL arrays (Gao et al., 2003; Zorin et al., 2003) and the CM array (Zhang et al., 2017) delineates low Vp and Vs anomalies in the shallow mantle beneath the Khentii Mountains and the Middle Gobi volcano, and so uplift and volcanism were both attributed to the upwelling of hot mantle. Additionally, observations of high heat flow (60-70 mW/m^2) (Khutorskoy and Yarmoluk, 1989), high Sn attenuation (He et al., 2017), and null measurements from SKS splitting (consistent with either weak or vertically oriented fabric in the mantle) (Qiang et al., 2017), are all consistent with the existence of hot mantle upwelling in this area, though the source of the upwelling is still debated. To the south, a deep, strong low-velocity structure in the upper mantle was imaged by teleseismic tomography from beneath the southeast corner of south-central Mongolia to beneath the Gobi Desert (Zhang et al., 2017). Zhang et al. (2017) interpret this anomaly to represent laterally flowing asthenospheric mantle associated with the subducting Pacific slab. Asthenospheric flow is also supported by shear wave splitting measurements of NW-SE trending fast polarization directions and relatively large splitting delay times in south-central Mongolia (Barruol et al., 2008; Qiang et al., 2017; Qiang and Wu, 2019).

The XA volcanic site is less well-studied than most of the other intraplate volcanoes in Eastern Asia. A “big mantle wedge” model beneath Eastern Asia, associated with the dehydration of the subducting Pacific slab, has been proposed to explain most if not all the volcanism in Eastern Asia by several large-scale regional tomographic studies (e.g., Zhao, 2004; Huang and Zhao, 2006). As for the Xilinhot-Abaga, body wave and surface wave tomographic studies showed low Vp and Vs anomalies with, at most, modest amplitudes in the uppermost mantle beneath this volcanic province (Tang et al., 2014; Guo et al., 2016a; Liu et al., 2017). Guo et al. (2016a) and Liu et al. (2017) attributed the low-velocity anomalies and surface volcanism to local asthenospheric upwelling induced by a mantle downwelling beneath the Songliao Basin to the east, which is a distinct mechanism from the “Big Mantle Wedge”.

Abundant geophysical and geochemical studies have been focused on the tectonic evolution of the NCC. Here, we focus on the TNCO and the western NCC. Body wave tomography revealed a prominent low-Vp anomaly in the upper mantle beneath the TNCO, attributed to asthenospheric upwelling (Tian et al., 2009). Petrological observations also imply asthenosphere upwelling which could be responsible for the magmatic events and widespread volcanic rocks in the Shanxi Graben (Deng et al., 1996; Xu et al., 2005). Meanwhile, the source of the Datong volcano is still a matter of debate. Several regional tomographic studies have suggested that Datong volcanism is driven by the dehydration of the subducted Pacific slab (Huang and Zhao, 2006; Tian et al., 2009). Alternatively, Lei (2012) proposed that a lower mantle plume drives the Datong volcanism from the observation that anomalies under the Datong volcano and Bohai Sea were connected to a broader anomaly that extends into the lower mantle.

Moving to the western NCC, the tectonically stable Ordos Block is characterized by low Bouguer gravity anomalies and low heat flow (40 mW/m^2) (Ma, 1989; Yuan, 1996; Hu et al., 2001; Zhai and Liu, 2003; Qiu et al., 2005). A recent GPS study found low deformation rates (a few nanostrain/yr or less) in the interior of the Ordos Block (Wang and Shen, 2020). Several seismological investigations suggested there is consensus as to the presence of very thick and cold lithosphere remaining beneath the Ordos Block (e.g., Tian et al., 2009; Lei, 2012; Tang et al., 2013; Gao et al., 2018). Moreover, the LAB as imaged by receiver function and surface wave tomography shallows northward from the Ordos Block towards the Yinshan orogen, and shallows eastward from the Ordos Block to the TNCO (Chen, 2010; Tang et al., 2013).

2. Data and Method

Intrinsic seismic attenuation is caused by energy absorption due to anelasticity (Nowick and Berry, 1972), and is quantified by the quality factor Q, defined as

$$\mathrm{Q}^{-1} = \frac{\Delta\mathrm{E}}{2\pi\mathrm{E_o}} \quad (1)$$

where $\Delta\mathrm{E}$ is the energy lost per cycle and $\mathrm{E_o}$ is the elastic energy in the wavefront. The amplitude spectrum $\mathrm{A}(\omega)$ of an attenuated signal is given by

$$\mathrm{A}(\omega) = \mathrm{A_0}(\omega)\mathrm{e}^{\frac{-\omega\mathrm{x}}{2\mathrm{Q}(\omega)\mathrm{c}(\omega)}} \quad (2)$$

where $\mathrm{A_0}(\omega)$ is the unattenuated spectrum, ω is the angular frequency, x is the traveled distance and $\mathrm{c}(\omega)$ is the phase velocity (Aki and Richards, 2002). The parameter t^* that represents the cumulative effect of Q over the entire body-wave path, is commonly used for seismic attenuation analysis and is defined as (Stein and Wysession, 2003)

$$t^* = \int \frac{dt}{Q} = \int \frac{dx}{c*Q} \quad (3)$$

where t is the travel-time in seconds. Teng (1968) developed a method for estimating the relative attenuation ($\Delta\mathrm{t}^*$) between the recordings of the same earthquake at two stations. This method calculates the relative attenuation from the ratio of the amplitude spectra from waveforms of the same event recorded by two stations. Later methods such as “reference/mean spectrum” (Adams and Humphreys, 2010; Cafferky and Schmandt, 2015), “pseudo source” (Boyd and Sheehan, 2005), and “common spectrum” (Halderman and Davis, 1991), are improved spectral methods to find the differential attenuation between all stations in an array simultaneously, without picking a reference station. In this study, we aim to characterize intrinsic seismic attenuation beneath our study area using a time-domain waveform-matching approach developed by Bezada (2017) based on the time-domain method of Adams and Humphreys (2010). We use a time-domain method rather than spectral methods because spectrum calculation and Δt^* estimation is sensitive to the subjectively chosen window of time and frequency range considered for the measurement (Adams and Humphreys, 2010; Bezada et al., 2019), and because time-domain methods allow for straight-forward quality control of the measurements. The time-domain waveform method has been applied successfully in Spain and Morocco (Bezada, 2017), Australia (Bezada and Smale, 2019), the Central Appalachian Mountains (Byrnes et al., 2019), and the Salton Trough (Byrnes and Bezada, 2020) yielding results that correlate well with previous geological and geophysical constraints.

2.1 Data Selection

We used data from three temporary broadband seismic arrays: The CM array with 69 stations installed in central Mongolia (August 2011-August 2013), the NM with 36 stations installed in Inner Mongolia, China near the XA volcanic province (October 2012-July 2015), and the OD array with 43 stations installed around the Ordos Block (May 2010-November 2011). These deployments have a typically station spacings of 30 to 60 km (Fig. 1).

We use teleseismic P phases from events with epicentral distance between 30° and 90°. We also choose events with hypocentral depths greater than 250 km in order to avoid the highly attenuating asthenosphere (e.g., Dziewonski and Anderson, 1981) on the source side. In this way, we maximize the effect of receiver-side structure on the attenuation signal. Furthermore, to ensure the events have enough energy to produce high signal-to-noise ratios, we restrict the event magnitudes to between Mb 5.5 and 7.3. Events in this magnitude range tend to have simple, impulsive and short-duration source time signatures (Hwang et al., 2011), making them amenable to our analysis.

We select a total of 38 events: 13 events recorded by the CM array, 14 events recorded by the NM array and 16 events recorded by the OD array (Fig. 2). Additionally, 2 of the events were recorded by both the CM and NM arrays, and 3 of them were recorded by both the CM and OD arrays. The analysis is carried out on vertical velocity seismograms. After removing the mean, trend, and instrument response (Haney et al., 2012), we filter the seismograms with a 4^{th} order Butterworth filter with corners at 0.02 and 3 Hz. We measured Δt^{*} on direct P-wave phases which have consistent, simple and impulsive appearance across the array.

2.2 Δt^{*} Estimation

The first step of the waveform matching method is to estimate a minimally attenuated source-time function for each event (Bezada, 2017). To do this, we select what appear to be the least-attenuated records, based on visual inspection. The main selection criterion is the duration of the recorded pulse. Less attenuated records will show more impulsive, shorter duration waveforms than the more attenuated ones owing to the progressive depletion of high frequencies with increasing attenuation. We then stack the least-attenuated traces to produce the source time function estimate (Fig. 3), (Bezada, 2017). This process is iterative, in that individual records are included and excluded from the stack until it is clear that only the least-attenuated waveforms are selected.

Synthetic waveforms are then generated by applying a linear operator $L(\omega)$ that models the effect of frequency-independent attenuation to the source estimate. The operator presented by Azimi et al. (1968) is defined in the frequency domain by:

$$L(\omega) = e^{-\omega t^{*}\left(\frac{1}{2}+\frac{i}{\pi}\ln\left(\frac{\omega}{\omega_0}\right)\right)} \quad (4)$$

where ω_0 is reference frequency. The choice of reference frequency only affects the arrival time and not the shape of waveform, making it inconsequential for this study (Bezada, 2017). The real and imaginary parts of (4) describe the attenuation and dispersion caused by anelasticity. We use equation 4 to numerically attenuate the source time function estimate and grid-search over t^{*} to find the value that minimizes the L2-norm of the difference between the observed and numerically attenuated waveforms. This is followed by a visual quality-control step where synthetic traces that do not conform to the observation are excluded from the analysis (Bezada, 2017). We remove the mean t^{*} for each event to produce relative attenuation measurements (Δt^{*}, hereafter), since we do not know the value of t^{*} associated with the source estimate. In this study, 829 Δt^{*} measurements were kept after quality control.

2.3 Inversion

To combine the Δt^{*} measurements into a statistically robust map, we use the Hierarchical Bayesian Monte Carlo inverse method (Bodin et al., 2012a, b) implanted by Byrnes et al. (2019).

One advantage of this approach is that free parameters related to regularization (such as smoothing and damping weights) are not needed, and the complexity of the solution is driven by the estimated uncertainty of input data. We first draw a starting model of 2-D (map view) relative attenuation from the prior, and then iteratively perturb the model in a way that maintains consistency with Bayes' theorem.

We ran 10 parallel chains of the search with independent starting models for 10^5 iterations, with a burn-in of $5x10^3$ iterations, and saved each 100^{th} model for analysis, as adjacent models will be not be sufficiently different to be of interest. A final model is constructed by averaging the values of the accepted models from all the chains interpolated onto a regular grid. At every point in the grid, an estimate of model uncertainty is given by the standard deviation of the values in the ensemble of accepted models.

2.4 Synthetic Tests

Combining relative attenuation data from three different arrays may pose challenges to the inversion. We do not constrain absolute t^*, and so events measured at different arrays will be separately demeaned. Before applying the inverse procedure to the data, we must ensure that the procedure is able to accurately recover anomalies that span different arrays without introducing artifacts at the array boundaries by performing a series of tests with synthetic data that is demeaned in the same way as the real data. In the first two tests, we attempt to recover smooth models of Δt^* across the entire study area. In these cases, Δt^* increase linearly with either longitude or latitude from 0 to 0.5 s (Fig. 5a and 5b). For the third input model, we set up a single rectangular anomaly with longitude and latitude boundaries of 40°N, 45°N, 108°E and

114°E, which intersects with all 3 arrays. Values of Δt^* inside and outside the rectangular anomaly are set to 0.5 s and 0 s, respectively (Fig. 5c). The synthetic data set contains the same configuration of station-evet pairs as the real data set. Δt^* values are taken from the input models described above, with the mean per event removed and with Gaussian white noise with a standard deviation of 0.075 s added.

We recover the overall character of the input models in all cases (Fig. 5). The range of the Δt^* are well-estimated, and gradational models can be easily distinguished from models with sharp discontinuities. The recovered data uncertainty in each case is 0.074 s, 0.078 s, and 0.075 s respectively, which are excellent matches to the standard deviation of the input Gaussian noise. These results give us confidence in the geometry and amplitude of the anomalies we image when inverting the real data set, without additional uncertainties introduced by using data from different arrays.

3. Results

We present our preferred model for lateral variations of Δt^* in Fig. 6a, with high or low attenuation anomalies labeled in the map as referred to in the following sections. The values of Δt^* in the preferred model range from -0.2 s to 0.2 s (Fig. 6a), and the standard deviation of the modeled values is typically in the range of 0.05 -0.07 s (Fig.6b). A uniform data uncertainty term was solved by the inversion (see Byrnes et al., 2019 for details) with mean value of 0.18 s.

3.1 Fundamental Features

The relative attenuation map of the study area can be described as showing a broad band of elevated attenuation running NNW-SSE from the Khentii Mountains to the Datong volcano, flanked by two prominent low attenuation regions: one to the east at 42-46°N coinciding with the Xilinhot-Abaga volcanoes, and another one to the west at 36-40°N coinciding with the Ordos Block (Fig. 6). Along the high-attenuation band, values are highest in the north, near the Khentii Mountains and the Middle Gobi volcano on the northeastern and southwestern edges of the area covered by the CM array (referred to as HA1 and HA2, respectively). There, Δt^* values reach 0.13-0.15 s (Fig. 6, 7d, 7e). To the south, the Gobi Desert shows values of ~0.09 s (HA4) and similar values are found continuing south all the way to the Datong volcano (HA3) (Fig. 6, 7d, 7e).

Low attenuation values are found in the XA volcanic province (LA2), with Δt^* reaching values of -0.15 s (Fig. 6, 7a, 7c, 7f). However, the uncertainty is large and increases towards the east. A sharp gradient in Δt^* separates LA2 from the higher attenuation to the west (HA3/HA4), whereas the transition from the high values in HA3 to the lowest attenuation values in the Ordos Block (LA1) is gradual (Fig. 6, 7b, 7c). Attenuation in the Ordos Block decreases from east to west, with the lowest attenuation being similar to that found beneath the XA volcanic province (Fig. 6, 7b, 7c). Again, however, uncertainties on the minimum values are large and grow towards the west.

3.2 Correlations with Other Observations

We consider our results in the context of lateral variations in topography, volcanism, and seismic velocity by presenting 6 cross-sections across the study area that traverse the main tectonic and volcanic provinces (Fig. 7). The seismic velocity model used a full waveform inversion of regional seismograms (Tao et al., 2018). In general, we expect high attenuation to coincide with low velocities in the mantle and low attenuation with high-velocity features, given the sensitivity of both these physical parameters to temperature (e.g., Goes et al., 2000; Cammarano et al., 2003) and the effect of anelasticity on velocity (Karato, 1993; Faul and Jackson, 2005). Previous studies with this type of attenuation constraint typically observe this general pattern (Byrnes et al., 2019; Bezada and Smale, 2019; Bezada, 2017), and we observe this anti-correlation here as well.

Positive velocities anomalies underlie the cratonic Ordos block, where we observed negative Δt^* anomalies (Fig. 7b and c). The mountain ranges further east show higher Δt^* values and low Vp and Vs anomalies (Fig. 7b and c). The HA1 and HA2 anomalies, two regions with higher attenuation near the Khentii Mountains and Middle Gobi volcano, are correlated with relatively high elevation and low velocity anomalies in the shallow mantle (Fig. 7d, e and f). A narrow low-velocity anomaly at depths shallower than 200 km underlies the rough, high topography of the Yinshan-Yanshan Orogenic Belt, where we found elevated attenuation in our model (Fig. 7c). In the eastern part of the Yinshan-Yanshan Orogenic Belt, we note a significant drop of Δt^* directly north of the mountains where the profiles cross into lower elevation (Fig. 7a, c, d and e). The Gobi Desert sits at relatively low elevation and is underlain by moderately high seismic velocity anomaly down to 200 km, and we find reduced but still positive Δt^* values (HA4).

Volcanic provinces are commonly associated with low-velocity anomalies in the subsurface, thinner lithosphere, the presence of melt, and high temperatures. Hence, the expected observation near volcanoes is high attenuation (e.g., Shapiro et al., 2000). Nevertheless, our Δt^* map does not show a consistent pattern of attenuation associated with regions exhibiting Cenozoic volcanism. First, the DT volcanic site is near the highest Δt^* values in HA3 and, as expected, is underlain by a high-amplitude low-velocity anomaly at depths up to 200 km (Fig. 6, 7a, 7b, 7d, 7e). However, the BO and MG volcanoes do not coincide with the northern extremum of Δt^* (Fig. 6, 7d, 7e, 7f), though they are in the province of the most positive values in the study area. Most surprising is the observation of some of the lowest Δt^* values near the XA volcanic province (Fig. 6, 7a, 7c, 7f).

To demonstrate the variable correlations between velocity and attenuation in our study, we compare our Δt^* results with $\Delta \mathrm{Vp}/\mathrm{Vp}$ at five different depths (Fig. 8) from the velocity model of Tao et al. (2018). In general, we find attenuation anti-correlates with velocity variations at depths from 100 to 200 km across the study area – as expected - except for LA2 region (Fig. 8). The largest correlation coefficients occur for depths from 100 to 150 km (Fig. 8b, c), with weak correlation at 50 km depth and essentially no correlation between velocity and attenuation at 300 km depth (Fig. 8d). The strong anti-correlation between attenuation and velocity is consistent with the sensitivity of both to temperature, and possibly melt and water (e.g., Goes et al., 2000; Cammarano et al., 2003). These observations support previous inferences that teleseismic attenuation is primarily sensitive to the subcrustal lithosphere-asthenosphere system (Kennett and Abdullah, 2011; Bezada and Smale, 2019; Byrnes and Bezada, 2020), while studies based on seismic velocity can interrogate structure within the crust and below the asthenosphere (Castaneda et al., in submission). The well-defined positive correlation at depths of 100-200 km beneath the LA2 region (Fig. 8b, c, d) is counter-intuitive and cannot be explained by thermal variations (e.g., Goes et al., 2000; Cammarano et al., 2003). In supplementary Section 1, we present an F-test to further show that the two-trend relation between velocity and attenuation in different regions at depths from 100 to 200 km is robust. The results of the F-test suggest that the attenuation and velocity across the study area are better fit by a two-trend model than by a single linear model with greater than 99% confidence even when the uncertainties on the attenuation results are considered (Fig. S1). We also note that between the HA3 and the HA1, HA2, and HA4 regions, large velocity variations at depths of 100 km occur without matching fluctuations in attenuation (Fig. 8), and so some decoupling between velocity and attenuation is likely real. We also note that while the model of Tao et al., (2018) is defined across the whole of Eastern Asia, the most negative Δt^* values in the LA2 region occur at the edge of the station coverage and rapidly become more negative as the edge of coverage is approached from west to east. Further studies are needed to confirm the lateral extent of negative Δt^* anomalies in the XA volcanic site.

3.3 Estimates of Absolute Qp

Since the 2D Δt^* model only gives the path-integrated attenuation, and given that our data are not sufficient to constrain a 3D tomographic model for Qp, we explore several hypothetical scenarios to estimate plausible values of Qp using a procedure similar to that applied in Byrnes et al. (2019) and Deng et al (2021). Qp values are estimated assuming a vertically propagating P wave from 200 km depth to the surface. We consider a two-layer model where the lithosphere and asthenosphere have constant Qp and the attenuation depends on the path length through each of the layers and the Qp values. We seek combinations of those parameters that are consistent with the observed differences in attenuation between LA1 (Δt^*= -0.04 ± 0.03 s) and HA1-HA2 (Δt^*= 0.11 ± 0.03 s), HA3-HA4 (Δt^*= 0.08 ± 0.03 s) and LA2 (Δt^*= -0.06 ± 0.06 s). We use the minimum values of Δt^* in LA1 that is robust against the uncertainties, as we noted above that the uncertainties grow towards west in LA1 (i.e., the Ordos block). Then equation (3) becomes

$$\Delta t^* - \Delta t^*_{LA1} = \left(\frac{t_{asth}}{Q_{p\_asth}} + \frac{t_{lithos}}{Q_{p\_lithos}}\right) - \left(\frac{t_{asth\_LA1}}{Q_{p\_asth\_LA1}} + \frac{t_{lithos\_LA1}}{Q_{p\_lithos\_LA1}}\right) \qquad (5)$$

where tlithos and tasth are the travel time through the lithosphere and ashenosphere, respectively. Qp_lithos and Qp_asth are the Qp values in the lithosphere and asthenosphere, respectively.

We first explore the case where we hold lithospheric thickness fixed to 200 km under the Ordos block (LA1 region) and 70 km elsewhere based on the thermomechanical model of Guo et al (2016b). Under these conditions, for any assumed value of lithospheric Qp, we can find the range of asthenosphere Qp that is consistent with our observed dt* and their uncertainties for any assumed value of lithospheric Qp. We find that an attenuating asthenosphere is required to explain the observations in regions HA1-HA2 and HA3-HA4 (Fig. 9a). Estimates for the two regions overlap considerably, spanning Qp values from 95 to 200 (Fig. 9a). Assuming that the Qp/Qs ratio is greater than 2, as expected (Karato and Speltzer, 1990) these values are within the range of globally average asthenosphere (e.g., Dziewonski and Anderson, 1981; Dalton et al., 2008, Dalton and Faul, 2010; Ma et al., 2020). Even at the more attenuating end of the results, Qp is markedly higher than observed in many volcanic zones (e.g., Abers et al., 2014; Pozgay et al., 2009; Wei and Wiens, 2020; Byrnes et al., 2019; Byrnes and Bezada, 2020). Our results suggest that Qp is lower in the north near the Middle Gobi and Bus Obo volcanoes than in the south beneath the Datong or Honggertu volcanoes, but this difference is not robust. A modest increase in temperature or hydration towards the north is therefore possible but not inferred here (Faul and Jackson, 2005). In contrast to the HA regions, this exercise shows that if the lithosphere beneath the XA volcanic site (LA2) is thin, a very high Qp asthenosphere would be required to explain our observations (Fig 8a).

The previous estimates assume a 70 km thick lithosphere outside of the Ordos Block, but variations are possible. Beneath HA1, HA2, and HA3, the estimates of asthenospheric Qp are likely robust (Guo et al., 2016b; Zhang et al., 2017; Tao et al., 2018), but Zhang et al. (2017) inferred a lithospheric thickness of approximately 100 km beneath the HA4 region. To explore the effect of variable lithospheric thickness below the HA regions we hold lithospheric Qp fixed to either 600 or 1400 (as plausible end members) and find the combinations of asthenosphere Qp and lithospheric thickness that are consistent with the observations in those regions. The asthenospheric Qp beneath HA4 spans from 80 to 140 if the lithospheric thickness equals 100 km (Fig. 9b). Assuming a 150 km thick lithosphere, the asthenospheric Qp beneath this region would be below 80, and so lower than the other HA regions (Fig. 9b).

We similarly explore the effect of different lithospheric thicknesses below LA2 (XA volcanic province). We find that the results can be explained with near-global-average values for asthenospheric Qp if the lithosphere beneath this region is ~150 km thick (Figure 8c). Our results then allow for two end-member possibilities for this region: the first is that the lithosphere is relatively thick, and the second is that the asthenosphere has higher Qp than the global average. Lithosphere as thick as beneath the Ordos block is allowed by the attenuation (Figure. 9c) but is likely inconsistent with seismic tomography (Fig. 7b and c). Instead, seismic tomography reveals modest high velocity anomalies that could reflect either modestly thick lithosphere or modestly cool asthenosphere, or some combination of the two, both of which are consistent with our observations (Fig. 9c). In any of these scenarios, we can reject the possibility of thin lithosphere underlain by normal asthenosphere, which distinguishes this region from the HA regions.

4. Discussion

We primarily interpret our results in terms of variations in lithospheric thickness and discuss the implications for magma genesis in Eastern Asia. Our results are consistent with a lithosphere-asthenosphere system with thick lithosphere beneath the Ordos block, moderately thick lithosphere beneath the XA volcanoes, and thin lithosphere in the rest of the study area. Where the lithosphere is thin, widespread volcanism occurs and the asthenosphere is as attenuating as the global average.

We make two inferences from these observations regarding the source of volcanism in this region. First, the volcanism in the HA regions that we observe do not require unusual asthenosphere conditions. We show above that Qp values beneath this region is approximately the same as in globally average asthenosphere. In contrast, lower Qp values are observed beneath volcanic regions where small-scale convection or subduction driven melting occurs (e.g., Abers et al., 2014; Pozgay et al., 2009; Wei and Wiens, 2020; Byrnes et al., 2019; Byrnes and Bezada, 2020), and markedly lower Qp values are inferred near the Hainan plume in South China (Deng et al., 2021). We show in supplementary Section 2 that while lower Qp values in the HA regions are estimated if a reference value in LA1 of -0.1 s is assumed, a value at the lower end of the uncertainty of the observations, the estimated Qp values are lower but still similar to the globally average asthenosphere (Fig. S2).

Instead, our results are consistent with the intraplate volcanism in this portion of Eastern Asia primarily tapping melt from the ambient asthenosphere. Isotopic evidence suggests that the widespread Cenozoic Mongolian volcanism is unlikely to involve a deep mantle upwelling, and that the magma source resides instead in the shallow asthenosphere (Barry et al., 2003, 2007). Petrological studies infer that the pressures of melts erupted at Datong are sourced from just below the base of a 60 km thick lithosphere (Xu et al., 2005), at which depths elevated temperatures are not required to explain melting. Many studies infer that the asthenosphere contains a small fraction of partial melt due to the presence of volatiles, even in region far from exceptional conditions such as mantle plume (e.g., Gaillard et al., 2008; Kawakatsu et al., 2009; Debayle et al., 2020). These melts may be able to reach the surface in a region of thin lithosphere or widespread fracturing, such as likely occurs beneath basin and range provinces (Plank and Forsyth, 2016) or in some subduction zones (Hirano et al., 2006).

While our results are consistent with ambient asthenospheric processes as a mechanism for volcanism, more active processes are allowed. Zhang et al. (2017) proposed that deep mantle upwelling occurs beneath HA4, and that lateral flow beneath the lithosphere feeds volcanism north and south of the Gobi Desert. Our results allow the lowest Qp in this region, since the lithosphere may be thicker than elsewhere (Zhang et al., 2017). The attenuation constraints thus are consistent with but do not require this mechanism. A “Big Mantle Wedge” related to subduction of the Pacific plate has also been invoked to explain volcanism. While our results do not require unusual asthenosphere conditions, the results are compatible with this model. For example, while melting beneath Datong volcano does not require elevated temperatures, enrichment in the source may have come from fluids released from the subducted slab (Xu et al., 2005).

In contrast, the observations require that the source of the magma feeding the XA field is deep. Our results admit two possibilities: Either the lithosphere is thicker beneath the XA region than beneath any of the HA regions, or the asthenospheric Qp is very high. In the high-Qp asthenosphere scenario, the low attenuation would be inconsistent with a mantle sufficiently close to the solidus to generate volcanism (e.g., Abers et al., 2014), and can thus be ruled out. The thicker lithosphere scenario is supported by petrologic models for melting in the XA region (Guo et al., 2020). Chen et al (2015b) show the volcanic rocks from XA have lower Na/Ti ratios than those from surrounding Cenozoic volcanic fields including Datong, indicating that XA volcanism may be characterized by the deepest melting and thickest lithosphere.

The hypothesis of a thicker lithosphere beneath XA may be inconsistent with previous seismic tomography studies (e.g., Tao et al., 2018). One possible explanation is that, as noted above, the negative tail of attenuation (Fig. 8e) at the XA volcanoes reflects the edge of our station coverage and may not be confirmed by future studies. However, observations of volcanic regions with low-velocity anomalies and low attenuation are not unprecedented. Low attenuation is observed beneath the volcanic provinces of Morocco and the Southeast Volcanic Province of Spain (Bezada, 2017) and the Yellowstone hot spot (Lawrence et al., 2006; Adams and Humphreys, 2010). Lawrence et al. (2006) and Adams and Humphreys (2010) proposed the presence of partial melt and consequent dehydration of lithosphere may account for the positive correlation of attenuation and velocity. However, the effects of water and partial melt on attenuation are still debated, with some experiments arguing a strong dependence on water but a weak dependence on melt (e.g., Karato, 2003; Shito et al., 2006), while others argue for a weak effect of water (Cline et al., 2018) and significant effect of melt (e.g., Chantel et al., 2016) and oxidation state (Cline et al., 2018). Given these uncertainties, we do not propose mechanism for the positive correlation here. However, whatever the mechanism, the structure of melting column beneath the XA volcanoes must be distinct from the other volcanoes in the region that exhibit the expected anti-correlation between velocity and attenuation. Our results do confidently show that regionally high temperatures or typical asthenosphere cannot be present beneath the XA volcanoes.

Thus, some mechanism enabling melting at depths greater than the either thick lithosphere or high-Qp asthenosphere beneath the XA volcanoes is likely required by the seismic observations. Melting beneath XA likely involves fluids released from the stagnant Pacific slab in the mantle transition zone (Chen et al., 2015b). A marked signal of a pyroxenite source and elevated $^{206}Pb/^{204}Pb$ ratios indicate a contribution from the crust of the recently subducted Pacific plate (Zhang and Guo, 2016). Alternatively, the retreating Pacific slab may drive melting by expelling material from the wet mantle transition zone into the water-poor upper or lower mantle (Yang and Faccenda, 2020). The XA is located in the south Xing'an-Mongolia Orogenic Belt, which places the XA volcanoes within the region where Yang and Faccenda (2020) hypothesize volcanism will occur through this mechanism, while the Datong, Middle Gobi, and Bus Obo sites are too far to the west.

5. Conclusion

Observations of teleseismic P wave attenuation provide new constraints for the genesis of volcanism beneath the Central Orogenic Belt and North China Craton. As expected, we found low attenuation beneath the Ordos block and generally high attenuation beneath many of the volcanic sites in the study area (e.g., the Middle Gobi volcano, the Bus Obo volcano and the Datong volcano). Counter-intuitive low attenuation, however, is revealed beneath the

Xilinhot-Abaga volcanic site. Absolute Qp values are estimated based on the relative attenuation constraints and previously observed variations in lithospheric thickness. Our results do not require unusual asthenosphere conditions for most of the volcanism in this portion of Eastern Asia. We infer that these volcanoes could be sourced from ambient asthenosphere and occur where the lithosphere is thin, though contribution from deeper sources of fluids are possible. In contrast, at the Xilinhot-Abaga volcanic site, our results exclude a typical shallow melting column, consistent with lithospheric thickness as the primary cause of variations in the composition of erupted lavas across the study area.

Acknowledgments

We thank everyone involved in instrumentation preparation and fieldwork. This study was financially supported by the National Natural Science Foundation of China (grant 41874112, 41674094) and the National Science Foundation (grant EAR-1827277) to the University of Minnesota. The first author has also been financially supported by the International Training Program from China Earthquake Administration and China Scholarship Council. Data of relative attenuation measurements, attenuation model and model standard deviation obtained in this study are available in supporting information Data Sets S1 or can be found at http://dx.doi.org/10.17632/vthcnhdnsn.1.

References

Abers, G. A., Fischer, K. M., Hirth, G., Wiens, D. A., Plank, T., Holtzman, B. K., et al. (2014). Reconciling mantle attenuation-temperature relationships from seismology, petrology, and laboratory measurements. Geochemistry, Geophysics, Geosystems, 15, 3521–3542.

Adams, D. C., & Humphreys, E. D., (2010). New constraints on the properties of the yellowstone mantle plume from p and s wave attenuation tomography. Journal of Geophysical Research: Solid Earth, 115(B12).

Aki, K., and P.G. Richards. 2002. Quantitative Seismology, 2nd edition, University Science Books, Sausalito, California, 700 pp.

Azimi, S.A., Kalinin, A.V., Kalinin, V.V., Pivovarov, B.L., 1968. Impulse and transient characteristics of media with linear and quadratic absorption laws. Izy. Phys. Solid Earth 2, 88-93.

Barry, T.L., Kent, R.W., 1998. Cenozoic magmatism in Mongolia and the origin of Central and East Asian basalts. In: Mantle Dynamics and Plate Interactions in East Asia. In: Geodynamics, vol. 27, pp. 347–364.

Barry, T.L., Saunders, A.D., Kempton, P.D., Windley, B.F., Pringle, M.S., Dorjnamjaa, D., Saandar, S., 2003. Petrogenesis of Cenozoic basalts from Mongolia: evidence for the role of asthenospheric versus metasomatized lithospheric mantle sources. J. Petrol. 44 (1), 55–91.

Barry, T.L., Ivanov, A.V., Rasskazov, S.V., Demonterova, E.I., Dunai, T.J., Davies, G.R., Harrison, D., 2007. Helium isotopes provide no evidence for deep mantle involvement in widespread Cenozoic volcanism across Central Asia. Lithos 95, 415–424.

Barruol, G., Deschamps, A., Déverchère, J., Mordvinova, V.V., Ulziibat, M., Perrot, J., Artemiev, A.A., Dugarmaa, T., Bokelmann, G.H.R., 2008. Upper mantle flow beneath and around the Hangay dome, Central Mongolia. Earth Planet. Sci. Lett. 274, 221–233.

Bezada, Maximiliano, J., (2017). Insights into the lithospheric architecture of iberia and morocco from teleseismic body-wave attenuation. Earth and Planetary Science Letters, 478, 14-26.

Bezada, M.J. and Smale, J., 2019. Lateral variations in lithospheric mantle structure control the location of intracontinental seismicity in Australia. Geophysical Research Letters, 46, 12,862-12,869.

Bezada, M.J., Byrnes, J.S., Eilon, Z.C., 2019. On the robustness of attenuation measurements on teleseismic P waves: insights from micro-array analysis of the 2017 North Korean nuclear test. Geophys. J. Int. 218, 573–585.

Bodin, T., Sambridge, M., Rawlinson, N., Arroucau, P., 2012a. Transdimensional to-mography with unknown data noise. Geophys. J. Int.189, 1536–1556.

Bodin, T., Sambridge, M., Tkalˇci´c, H., Arroucau, P., Gallagher, K., Rawlinson, N., 2012b. Transdimensional inversion of receiver functions and surface wave dispersion. J. Geophys. Res., Solid Earth117.

Boyd, O. S., and A. F. Sheehan (2005), Attenuation tomography beneath the Rocky Mountain Front: Implications for the physical state of the upper mantle, in The Rocky Mountain Region: An Evolving Lithosphere, Geophys. Monogr. Ser., vol. 154, edited by K. E. Karlstrom and G. R. Keller, pp. 361–377.

Byrnes, J.S., Maximiliano Bezada, Maureen D. Long, Margaret H. Benoit, 2019. Thin lithosphere beneath the central Appalachian Mountains: Constraints from seismic attenuation beneath the MAGIC array. Earth and Planetary Science Letters, 519: 297-307.

Byrnes, J. S., & Bezada, M. (2020). Dynamic upwelling beneath the Salton Trough imaged with teleseismic attenuation tomography. Journal of Geophysical Research: Solid Earth, 125.

Cafferky, S., & Schmandt, B. (2015). Teleseismic P wave spectra from USArray and implications for upper mantle attenuation and scattering. Geochemistry, Geophysics, Geosystems, 16, 3343-3361.

Castaneda, Roque & Abers, Geoffrey & Eilon, Zachary & Christensen, D. (2021). Teleseismic attenuation, temperature, and melt of the upper mantle in the Alaska subduction zone. 10.1002/essoar.10505839.1.

Chantel, J. et al. (2016). Experimental evidence supports mantle partial melting in the asthenosphere. *Sci. Adv*. 2, e1600246.

Chen, L. (2010), Concordant structural variations from the surface to the base of the upper mantle in the North China Craton and its tectonic implications, Lithos, 120(1–2), 96–115.

Chen, M., Niu, F., Liu, Q., Tromp, J., 2015a. Mantle-driven uplift of Hangai Dome: new seismic constraints from adjoint tomography. Geophys. Res. Lett. 42 (17), 6967–6974.

Chen S S, Fan Q C, Zou H B, Zhao Y W, Shi R D. 2015b. Magma source and cause of late Cenozoic basaltic magma in Inner Mongolia, eastern China: Combined geochemical and isotope constrains. Journal of Volcanology and Geothermal Research, 305, 30–44.

Cline, C. J., Faul, U. H., David, E. C., Berry, A. J. & Jackson, I. (2018). Redox-influenced seismic properties of upper-mantle olivine. *Nature* 555, 355–358.

Dalton, C.A., Ekström, G., Dziewonski, ´ A.M., 2008. The global attenuation structure of the upper mantle. J. Geophys. Res., Solid Earth 113, B09303.

Dalton, C.A., Faul, U.H., 2010. The oceanic and cratonic upper mantle: clues from joint interpretation of global velocity and attenuation models. In: The Lithosphere/Asthenosphere Boundary: Nature, Formation and Evolution, Session EIL-03 of the International Geological Congress. Lithos 120, 160–172.

Debayle E., Bodin T., Stéphanie Durand, et al. (2020). Seismic evidence for partial melt below tectonic plates. Nature, Vol586, 555-559.

Deng, Q.D., Cheng, S.P., Min, W., et al., 1999. Discussion on Cenozoic tectonics and dynamics of Ordos block. J. Geomech. 5 (3), 13–21 (in Chinese).

Deng, J.F., Mo, X.X., Zhao, H.L., Wu, Z.X., Luo, Z.H., Su, S.G., 2004. A new model for the dynamic evolution of Chinese lithosphere: 'continental roots'–plume tectonics. Earth-Sci. Rev. 65, 223–275.

Deng Y. F., Byrnes, J. S., Bezada, M.J., 2021. New insights into the heterogeneity of the lithosphere-asthenosphere system beneath South China from teleseismic body-wave attenuation. Geophysical Research Letters, accepted.

Dziewonski, A.M., Anderson, D.L., 1981. Preliminary reference Earth model. Phys. Earth Planet. Inter. 25, 297–356.

Dziewonski, A.M., J. Stein, 1982. Dispersion and attenuation of mantle waves from waveform inversion. Geophys. J. R. Astr. Soc., 70, 503-527.

Faul UH, Jackson I. 2005. The seismological signature of temperature and grain size variations in the upper mantle. Earth Planet. Sci. Lett. 234:119–34.

Gaillard, F., Malki, M., Iacono-Marziano, G., Pichavant, M., & Scaillet, B. (2008). Carbonatite melts and electrical conductivity in the asthenosphere. Science, 322(5906), 1363-1365.

Gao, S., Davis, P.M., Liu, H., Slack, P.D., Zorin, Y.A., Mordvinova, V.V., Kozhevnikov, V.M., Meyer, R.P., 1994. Seismic anisotropy and mantle flow beneath the Baikal rift zone. Nature 371, 149–151.

Gao, S.S., Liu, K.H., Davis, P.M., Slack, P.D., Zorin, Y.A., Mordvinova, V.V., Kozhevnikov, V.M., 2003. Evidence for small-scale mantle convection in the upper mantle beneath the Baikal rift zone. J. Geophys. Res. 108 (B4), 2194.

Gao X, Guo B, Chen J H, et al. 2018. Rebuilding of the lithosphere beneath the western margin of Ordos: Evidence from multiscale seismic tomography. Chinese J. Geophys. 61(7), 2736-2749 (in Chinese).

Goes, S., Govers, R., & Vacher, P., (2000). Shallow mantle temperatures under europe from p and s wave tomography. Journal of Geophysical Research Solid Earth, 105(B5), 11153-11169.

Griffin, W.L., Andi, Z., O'Reilly, S.Y., Ryan, C.G., 1998. Phanerozoic evolution of the lithosphere beneath the Sino-Korean Craton. In: Flower, M. (Ed.), Mantle Dynamics and Plate Interaction in East Asia. In: Geodyn. Ser., vol. 27, pp. 107–126.

Gomer, RM., and E.A. Okal, 2003. Multiple-ScS probing ofthe Ontong-Java Plateau. Physics of the Earth and Planetary Interiors 138, 317-331.

Guo, Z., Chen, Y. J., Ning, J., Yang, Y., Afonso, J. C., & Tang, Y., et al. (2016a). Seismic evidence of on-going sublithosphere upper mantle convection for intra-plate volcanism in northeast china. Earth & Planetary Science Letters, 433, 31-43.

Guo, Z., Afonso, J. C., Qashqai, M. T., Yang, Y., & Chen, Y. J. (2016b). Thermochemical structure of the north china craton from multi-observable probabilistic inversion: extent and causes of cratonic lithosphere modification. Gondwana Research., 37, 252-265.

Guo, P., et al., 2020, Lithosphere thickness controls continental basalt compositions: An illustration using Cenozoic basalts from eastern China: Geology, v. 48, p. 128–133,

Halderman, T. P., & Davis, P. M., (1991). Q p beneath the rio grande and east african rift zones. Journal of Geophysical Research Atmospheres, 961(B6), 10113-10128.

Hammond, W.C., and Humphreys, E.D., 2000. Upper mantle seismic wave attenuation: Effects of realistic partial melt distribution, Journal of Geophysical Research, 105 (B5), 10987–10999.

Haney, M. M., Power, J., West, M., & Michaels, P. (2012). Causal Instrument Corrections for Short-Period and Broadband Seismometers. Seismological Research Letters, 83(5), 834–845.

He, J., Wu, Q., Sandvol, E., Ni, J., Gallegos, A., Gao, M., Ulziibat, M., Demberel, S., 2016. The crustal structure of south-central Mongolia using receiver functions. Tectonics 35.

He, J., Sandvol, E., Wu, Q., Gao, M., Gallegos, A., Ulziibat, M., Demberel, S., 2017. Attenuation of regional seismic phases (Lg and Sn) in Eastern Mongolia. Gepphys. J. Int. 211, 1001-1011.

Hirano, N., Takahashi, E., Yamamoto, J., Abe, N., Ingle, S. P., & Kaneoka, I., et al. (2006). Volcanism in response to plate flexure. Science, 313(5792), 1426-1428.

Ho K S，Liu Y，Chen J C，Yang H J. 2008. Elemental and Sr-Nd-Pb isotopic compositions of late Cenozoic Abaga basalts, Inner Mongolia: Implications for petrogenesis and mantle process. Geochemical Journal, 42, 339－357.

Hu, S., He, L., Wang, J., 2001. Compilation of heat flow data in the China continental area (3rd edition). Chin. J. Geophys. 44, 611–622 (in Chinese).

Huang J, Zhao D. 2006. High-resolution mantle tomography of China and surrounding regions. Journal of Geophysical Research, 111, B09305.

Hunt, A.C., Parkinson, I.J., Harris, N.B.W., Barry, T.L., Rogers, N.W., Yondon, M., 2012. Cenozoic volcanism on the Hagai Dome, Central Mongolia: geochemical evidence for changing melt sources and implications for mechanisms of melting. J. Petrol. 53 (9), 1913–1942.

Hwang, Y.K., Ritsema, J., Goes, S., 2011. Global variation of body-wave attenuation in the upper mantle from teleseismic P wave and S wave spectra. Geophys. Res. Lett. 38, L06308.

Karato, S., Spetzler, H.A., 1990. Defect microdynamics in minerals and solid-state mechanisms of seismic wave attenuation and velocity dispersion in the mantle. Rev. Geophys. 28, 399–421.

Karato, S. (1993), Importance of anelasticity in the interpretation of seismic tomography, Geophys. Res. Lett., 20, 1623-1626.

Karato, S. (2003), Mapping water content in the upper mantle, in Inside the Subduction Factory, Geophys. Monogr. Ser, vol. 138, edited by J. Eiler, pp. 135-152, AGU, Washington, D.C.

Kawakatsu, H., Kumar, P., Takei, Y., Shinohara, M., Kanazawa, T., & Araki, E., et al. (2009). Seismic evidence for sharp lithosphere-asthenosphere boundaries of oceanic plates. Science, 324(5926), 499-502.

Kennett, B. L. N., & Abdullah, A. (2011). Seismic wave attenuation beneath the Australasian region. Australian Journal of Earth Sciences, 58(3), 285–295.

Khutorskoy, M. D., and Yarmoluk, V. V., 1989. Heat flow, structure and evolution of the lithosphere of Mongolia. Tectonophysics, 164(2-4): 315-322.

Kononova, V.A., Kurat, G., Embey-Isztin, A., Pervov, V.A., Koeberl, C., Brandstaetter, F., 2002. Geochemistry of metasomatised spinel peridotite xenoliths from the Dariganga Plateau, South-eastern Mongolia. Mineral. Petrol. 75, 1–21.

Lawrence, Jesse F., Shearer, Peter M., & Masters, Guy., 2006. Mapping attenuation beneath north america using waveform cross-correlation and cluster analysis. Geophysical Research Letters, 33(7), L07315.

Lei, J. (2012), Upper-mantle tomography and dynamics beneath the North China Craton. J. Geophys. Res., 117, B06313.

Li, C., Van der Hilst, R.D., 2010. Structure of the upper mantle and transition zone beneath Southeast Asia from traveltime tomography. J. Geophys. Res. 115, B07308.

Li, S.Z., Zhao, G.C., Dai, L.M., Liu, X., Zhou, L.H., Santosh, M., Suo, Y.H., 2012. Mesozoic basins in eastern China and their bearing on the deconstruction of the North China Craton. J. Asian Earth Sci. 47, 64–79.

Li, Y.H., Wu, Q.J., Pan, J.T., Zhang, F.X., Yu, D.X., 2013. An upper-mantle S-wave velocity model for East Asia from Rayleigh wave tomography. Earth Planet. Sci. Lett. 377–378, 367–377.

Liu, D., A. Nutman, W. Compston, J. Wu, and Q. Shen (1992), Remnants of 3800 Ma crust in Chinese part of the Sino-Korean craton, Geology, 20, 339–342.

Liu, Yaning, Niu, Fenglin, Chen, Min, & Yang, Wencai., et al. (2017). 3-d crustal and uppermost mantle structure beneath ne china revealed by ambient noise adjoint tomography. Earth & Planetary Science Letters, 461, 20-29.

Ma, X.Y. (Ed.), 1989. Lithospheric Dynamic Atlas of China. Cartographic Publishing House, Beijing.

Ma, Z., Dalton, C. A., Russell, J. B., Gaherty, J. B., Hirth, G., & Forsyth, D. W. (2020). Shear attenuation and anelastic mechanisms in the central Pacific upper mantle. Earth and Planetary Science Letters, 536, 116148.

Molnar, P., Tapponnier, P., 1975. Cenozoic tectonics of Asia: effects of a continental collision. Science 189 (4201), 419–426.

Molnar, P., Deng, Q., 1984. Faulting associated with large earthquakes and the average rate of deformation in central and eastern Asia. J. Geophys. Res., Solid Earth 89, 6203–6227.

Molnar, P., England, P.C., Martinod, J., 1993. Mantle dynamics, uplift of the Tibetan Plateau and the Indian monsoon. Rev. Geophys. 31, 357–396.

Mordvinova, V.V., Deschamps, A., Dugarmaa, T., Deverchére, J., Ulziibat, M., Sankov, V.A., Artem'ev, A.A., Perrot, J., 2007. Velocity structure of the lithosphere on the 2003 Mongolian-Baikal transect from SV waves. Izv. Phys. Solid Earth 43, 119–129.

Nowick, A.S., and B.S. Berry. 1972. Anelastic relaxation in crystalline solids. Academic, San Diego, 667p.

Plank, T., and D. W. Forsyth (2016). Thermal structure and melting conditions in the mantle beneath the Basin and Range province from seismology and petrology, Geochem. Geophys. Geosyst., 17, 1312–1338.

Pozgay, S. H., Wiens, D. A., Conder, J. A., Shiobara, H., & Sugioka, H. (2009). Seismic attenuation tomography of the Mariana subduction system: Implications for thermal structure, volatile distribution, and slow spreading dynamics. Geochemistry, Geophysics, Geosystems, 10, Q04X05.

Priestley, K., Debayle, E., McKenzie, D., Pilidou, S., 2006. Upper mantle structure of eastern Asia from multimode surface waveform tomography. J. Geophys. Res. 111, B10304.

Qiang, Z., Wu, Q., Li, Y., Gao, M., Demberel, S., et al. (2017). Complicated seismic anisotropy beneath south-central Mongolia and its geodynamic implications. Earth and Planetary Science Letters, 465, 126–133.

Qiang, Z., Wu, Q., 2019. Upper mantle anisotropy beneath Abaga area in Inner-Mongolia from shear wave splitting. Chinese J. Geophys. 62(7), 2510-2526 (in Chinese).

Qiu, R.Z., Deng, J.F., Zhou, S., Li, J.F., Xiao, Q.H., Wu, Z.X., Liu, C., 2005. Lithosphere types in North China: evidence from geology and geophysics. Sci. China, Ser. D, Earth Sci. 48 (11), 1809–1827.

Ren, J., K. Tamaki, S. Li, and J. Zhang (2002), Late Mesozoic and Cenozoic rifting and its dynamic setting in eastern China and adjacent areas, Tectonophysics, 344, 175–205.

Schellart, W.P., Lister, G.S., 2005. The role of the East Asian active margin in widespread extensional and strike-slip deformation in East Asia. J. Geol. Soc. 162, 959–972.

Shapiro, N.M., Singh, S.K., Iglesias-Mendoza, A., Cruz-Atienza, V.M., Pacheco, J.F., 2000. Evidence of low-Q below Popocatepetl volcano, and its implication to seismic hazard in Mexico City. Geophys. Res. Lett., 27, 2753-2756.

Shito, A., Karato, S.-i., Matsukage, K. N. & Nishihara, Y. (2006). in *Earth's Deep Water Cycle* (eds Jacobsen, S. D. & Van Der Lee, S.) 255–236, AGU, Washington, D.C.

Stein, S., and M. E. Wysession (2003), An introduction to seismology, earthquakes, and Earth structure, 498 pp., Blackwell Publishing, Malden, Mass.

Tang, Y., Y. J. Chen, S. Zhou, J. Ning, and Z. Ding (2013), Lithosphere structure and thickness beneath the North China Craton from joint inversion of ambient noise and surface wave tomography, J. Geophys. Res. Solid Earth, 118, 2333–2346.

Tang, Y., Obayashi, M., Niu, F., Grand, S. P., Chen, Y. J., & Kawakatsu, H., et al. (2014). Changbaishan volcanism in northeast china linked to subduction-induced mantle upwelling. Nature Geoscience, 7(6), 470-475.

Tapponnier, P., Xu, Z., Roger, F., Meyer, B., Arnaud, N., Wittlinger, G., Yang, J., 2001. Oblique stepwise rise and growth of the Tibet Plateau. Science 294, 1671–1677.

Tao, K., Grand, S. P., & Niu, F. (2018). Seismic structure of the upper mantle beneath eastern Asia from full waveform seismic tomography. Geochemistry, Geophysics, Geosystems, 19, 2732–2763.

Teng, T.-L., 1968. Attenuation of body waves and the Q structure of the mantle. J. Geophys. Res. 73, 2195–2208.

Tian, Y., D. Zhao, R. Sun, and J. Teng (2009), Seismic imaging of the crust and upper mantle beneath the North China Craton, Phys. Earth Planet. Inter., 172, 169–182.

Walker, R.T., Nissen, E., Molor, E., Bayasgalan, A., 2007. Reinterpretation of the active faulting in central Mongolia. Geology 35 (8), 759–762.

Wang, F., Zhou, X., Zhang, L., Ying, J., Zhang, Y., Wu, F., & Zhu, R. (2006). Late Mesozoic volcanism in the Great Xing'an Range (NE China): Timing and implications for the dynamic setting of NE Asia. Earth and Planetary Science Letters, 251(1-2), 179–198.

Wang, M., & Shen, Z-K. (2020). Present-day crustal deformation of continental China derived from GPS and its tectonic implications. Journal of Geophysical Research: Solid Earth, 125.

Wei, S. S., & Wiens, D. A. (2020). High bulk and shear attenuation due to partial melt in the Tonga-Lau back-arc mantle. Journal of Geophysical Research: Solid Earth, 125.

Windley, B.F., Allen, M.B., 1993. Mongolian plateau: evidence for a late Cenozoic mantle plume under central Asia. Geology 21, 295–298.

Windley, B. F., Alexeiev, D., Xiao, W., et al., 2007. Tectonic models for accretion of the Central Asian Orogenic Belt. Journal of the Geological Society, 164(1), 31-47.

Xu, X., Ma, X., 1992. Geodynamics of the Shanxi rift system, China. Tectonophysics 208, 325–340.

Xu, Y.G., 2001. Thermo-tectonic destruction of the Archean lithospheric keel beneath eastern China: Evidence, timing, and mechanism. Phys. Chem. Earth (A) 26, 747–757.

Xu, Y., J. Ma, F. Frey, M. Feigenson, and J. Liu (2005), Role of lithosphere-asthenosphere interaction in the genesis of Quaternary alkali and tholeiitic basalts from Datong, western North China Craton, Chem. Geol., 224, 247–271.

Yang, Jianfeng and Faccenda, Manuele. (2020). Intraplate volcanism originating from upwelling hydrous mantle transition zone. Nature, Vol579, 88-91.

Ye, H., Zhang, B., Mao, F., 1987. The Cenozoic tectonic evolution of the Great North China: two types of rifting and crustal necking in the Great North China and their tectonic implications. Tectonophysics. 133, 217–227.

Yuan, X, 1996. Velocity structure of the Qinling lithosphere and mushroom cloud model. Sci. China (Ser. D) 39, 235–244.

Zhai, M.G., Liu, W.J., 2003. Paleoproterozoic tectonic history of the North China Craton: a review. Precambrian Res. 122, 183–199.

Zhang, Maoliang and Guo, Zhengfu. (2016). Origin of Late Cenozoic Abaga-Dalinuoer basalts, eastern China: Implications for a mixed pyroxenite-peridotite source related with deep subduction of the Pacific slab. Gondwana Research., 37, 130-151.

Zhang, F., Wu, Q., Grand, S. P., Li, Y., Gao, M., Demberel, S., et al. (2017). Seismic velocity variations beneath central Mongolia: Evidence for upper mantle plumes? Earth and Planetary Science Letters, 459, 406–416.

Zhao D P. (2004). Global tomographic images of mantle plumes and subducting slabs: insight into deep earth dynamics. Physics of the Earth & Planetary Interiors, 146, 3-34.

Zhao, G.C., Sun, M., Wilde, S.A., Li, S., 2005. Late Archean to Paleoproterozoic evolution of the North China Craton: key issues revisited. Precambrian Res. 136, 177–202.

Zorin, Y.A., Turutanov, E.K., Mordvinova, V.V., Kozhevnikov, V.M., Yanovskaya, T.B., Treussov, A.V., 2003. The Baikal rift zone: the effect of mantle plumes on older structure. Tectonophysics 371, 153–173.

Figure caption

Fig. 1. Map of study area and station distribution. Upper panel shows an overall view of Eastern Asia with our study area indicated by the black rectangle. Bottom panel gives tectonic features of the study area in detail, where the red triangles denote volcanoes, red stars are cities and thick dark grey lines represent outline tectonic provinces. The dashed white lines delineate boundaries among tectonic blocks labeled by white words. The yellow circles, squares and triangles are seismic stations from the OD array, NM array and CM array respectively. Abbreviations of tectono-magmatic features are: ALSB – Alashan Block, CAOB – Central Orogenic Belt, NCC – North China Craton, DT – Datong, HG – Honggeertu, DG – Dariganga, MG – Middle Gobi, BO – Bus Obo.

Fig. 2. Distribution of used events data received by three arrays respectively. The black triangle, square and circle represent locations of the CM array, NM array and OD array respectively. Circles are events. Color denotes focal depth and size denotes magnitude.

Fig. 3. Example of P phases used to construct a source estimate for one event recorded by the NM array. This event occurred in Tonga-Fiji subduction zone on 28 April 2015, with a magnitude of Mb 6.1, epicentral distance of 89° and focal depth of 580 km. Black curves in (a) are vertical

velocity seismograms showing the first-arriving P phase. Thick lines are traces picked for the estimated source-time function with their station names on the top right corner. In (b), blue, brown and yellow curves are selected traces from (a), recorded at stations NM11, NM13 and NM39 respectively. The dashed and solid red line denotes reference source trace within and without the fitting window.

Fig. 4. Example of waveform-matching and quality control for the event in Fig. 3. a). Black lines are observed seismograms, red lines are synthetic seismograms (cf. Fig. 3). b). The dashed and solid red line in panel (b) denotes synthetic traces within and without the fitting window. The result of station NM04 shown in panel (b) did not pass the quality control.

Fig. 5. Input and output models of synthetic tests. Figure (a1) and (b1) show the synthetic input models linearly increasing with longitude and latitude, respectively. Figure (c1) represents the synthetic input model with a fixed frame. Figure (a2), (b2), (c2) show the input Δt^* values which are demeaned. Figure (a3), (b3) and (c3) are demeaned results of three synthetic tests, respectively. Triangles, squares and circles are seismic stations, the same as shown in Fig. 1.

Fig. 6. Preferred inversion for $\Delta \mathbf{t}^*$. a). Δt^*, marked by color, four high-attenuation anomalies and two low-attenuation anomalies mentioned in the paper are labeled HA1, HA2, HA3, HA4 and LA1, LA2 respectively, and identified by thick black lines. Thick grey lines denote the location of six profiles shown in Fig. 7. b). Standard deviation of the Δt^* model in panel (a), is presented in this panel. Seismic stations and volcanoes are shown in by black dots and purple triangles, respectively.

Fig. 7. Comparison of geophysical observations along six profiles. Four panels of each profile are surface elevation, relative attenuation, Vp and Vs perturbation from top to bottom respectively. Velocity perturbation is extracted from the velocity model beneath Eastern Asia presented by Tao et al. (2018). Locations of the six profiles are shown in Fig. 7. Abbreviations in topographic map are: DT – Datong volcano, YYOB - Yinshan-Yanshan Orogenic Belt, XA – Xilinhot-Abaga volcanic site, MG – Middle Gobi vocalno, HM – Khentii Mountains, BO – Bus Obo volcano. HA1-4 and LA1-2 are labeled high or low-attenaution anomalies disscused in the paper and explained in Fig. 6.

Fig. 8. $\Delta \mathbf{Vp}/\mathbf{Vp}\%$ at different depths versus $\Delta \mathbf{t}^*$ values. We sample ΔVp% values of different regions at different depths ranging from 50-300 km from the velocity model of Tao et al. (2018), and then plotted them versus our Δt^* results to show the relation between attenuation and velocity. Points are sampled with a space interval of 50 km, which is bigger than the resolution (40 km*40 km*40 km) of the velocity model of Tao et al. (2018). In all the panels, blue, black, red, pink, and green squares denote samples from LA1, LA2, HA3, HA4, and HA1-2 (HA1 & HA2) regions. The size of squares are scaled by the inverse of the uncertainty of Δt^* values. Black lines represent linear regression results using samples from all the regions except for LA2, with correlation coefficients and slopes shown as black words on the top right corner. Brown lines represent linear regression results using samples from LA2, with correlation coefficients and slopes shown as brown words on the top right corner. All the regressions are weighted by the uncertainty of Δt^* results in this study.

Fig. 9. Qp estimates assuming two layers beneath different regions. Panel (a): Range of Qp beneath HA1, HA2, HA3, HA4, and LA2 regions, assuming a lithosphere with a 200 km thickness beneath LA1 as a reference, and 70 km thickness beneath the other regions. The grey part above the black line denotes where asthenospheric Qp is larger than lithospheric Qp, which are hypotheses considered unfeasible. Yellow dashed line represents the asthenospheric Qp from PREM (Dziewonski and Anderson, 1981), and the cyan dashed line represents the globally average asthenosphere Qp from Dalton et al. (2010). Green, red and black dashed lines denote observed lower asthenospheric Qp values from Abers et al. (2014), Byrnes et al. (2019) and Wei and Wiens (2018). Values are calculated assuming a Qp/Qs ratio of 2.25 (Karato and Spetzler, 1990). Panel (b): Range of asthenospheric Qp for different lithospheric thicknesses beneath HA4 region, assuming that lithospheric Qp equals 600 and 1400, respectively. Panel (c): Range of asthenospheric Qp varing with lithospheric thickness beneath the LA2 region, assuming lithospheric Qp equals 1400.

Fig. 10. Cartoon illustrating the relationship between volcanism and lithospheric thickness. In the left panel, the black line delineates an "N"-shaped transect in the study area, and the pink triangles are volcanoes. The volcanoes and abbreviations are the same as in Fig. 1. In the right panel, a cartoon illustrating the main interpretation of this study is shown along the "N"-shaped transect. Green dashed line denotes a mean LAB inferred from Guo et al. (2016b). Black thick line is an inferred LAB from our results, and the black thin line is surface topography. Seafoam wavy lines denote fluids or/and oceanic crust in the asthenosphere inferred from Zhang and Guo (2016) and Yang and Faccenda (2019). Dark blue block denotes the ~200 km thick lithosphere beneath the Orodos block inferred from Guo et al. (2016). Red thin arrows represent the path of ascent

for magma to the surface. Red thick arrow denotes the possibility of deep upwelling beneath the Gobi Desert if the lithosphere is thicker beneath this region. Red triangles are volcanoes. The abbreviations and volcanoes are the same as in Fig. 1.

Fig 1.

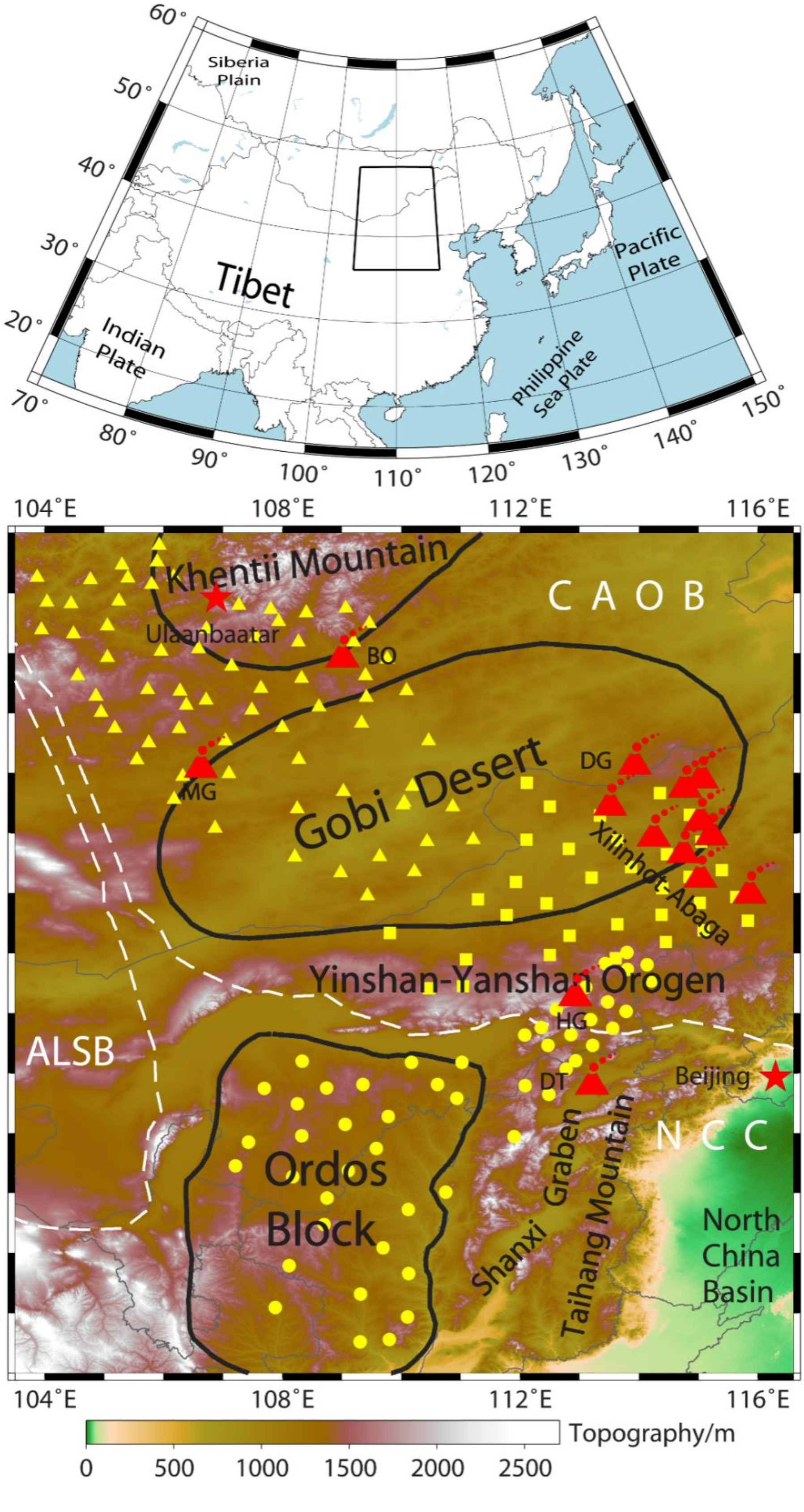

60°
50°
40°
30°
20°
70°
80°
90°
100°
110°
120°
130°
140°
150°
Siberia Plain
Tibet
Indian Plate
Pacific Plate
Philippine Sea Plate
104°E
108°E
112°E
116°E
48°N
44°N
40°N
36°N
Khentii Mountain
Ulaanbaatar
C A O B
BO
MG
DG
Gobi Desert
Xilinhot-Abaga
Yinshan-Yanshan Orogen
HG
DT
ALSB
Beijing
N C C
Ordos Block
Shanxi Graben
Taihang Mountain
North China Basin
Topography/m
0
500
1000
1500
2000
2500

Fig 2.

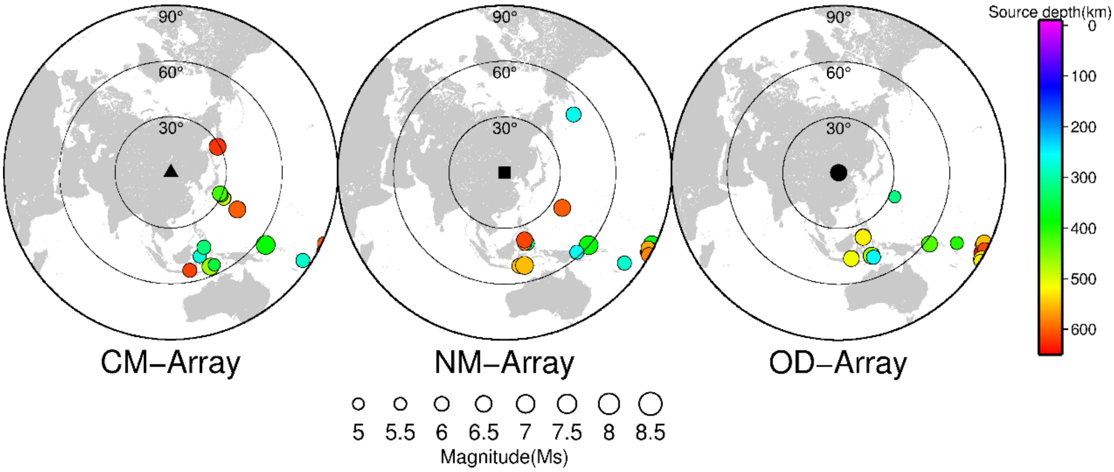
90°
60°
30°
CM–Array
NM–Array
OD–Array
Source depth(km)
0
100
200
300
400
500
600
5
5.5
6
6.5
7
7.5
8
8.5
Magnitude(Ms)

Fig 3.

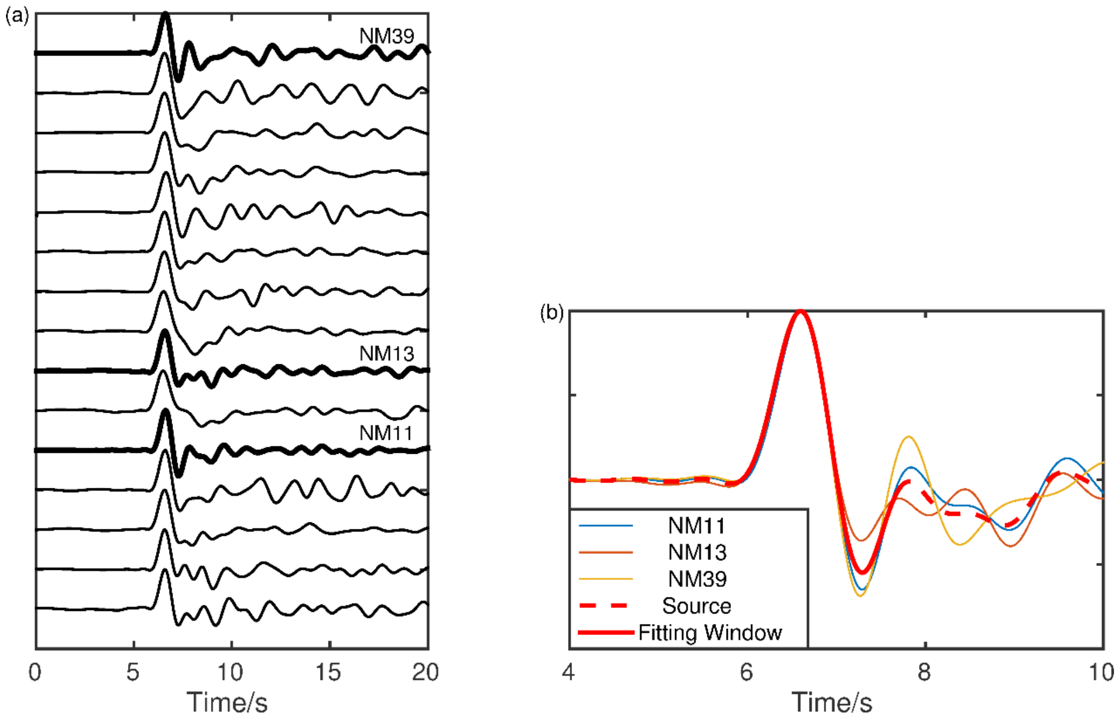
(a)
NM39
NM13
NM11
0
5
10
15
20
Time/s
(b)
NM11
NM13
NM39
Source
Fitting Window
4
6
8
10
Time/s

Fig 4.

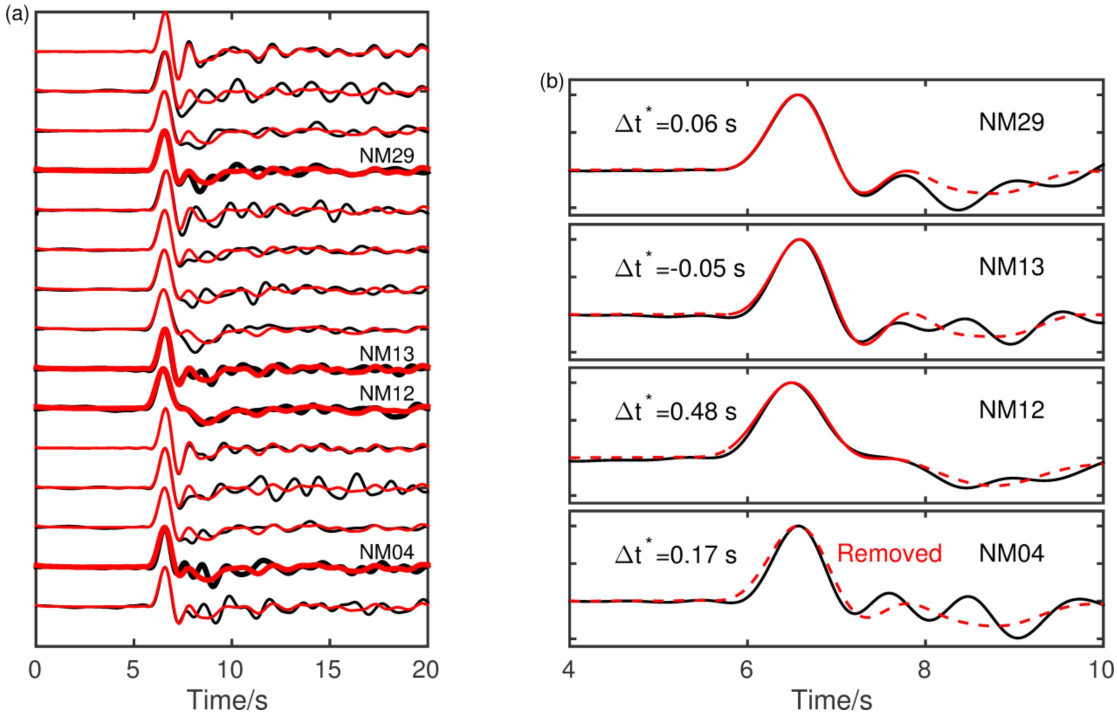
(a)
NM29
NM13
NM12
NM04
0
5
10
15
20
Time/s
(b)
Δt*=0.06 s
NM29
Δt*=-0.05 s
NM13
Δt*=0.48 s
NM12
Δt*=0.17 s
Removed
NM04
4
6
8
10
Time/s

Fig 5.

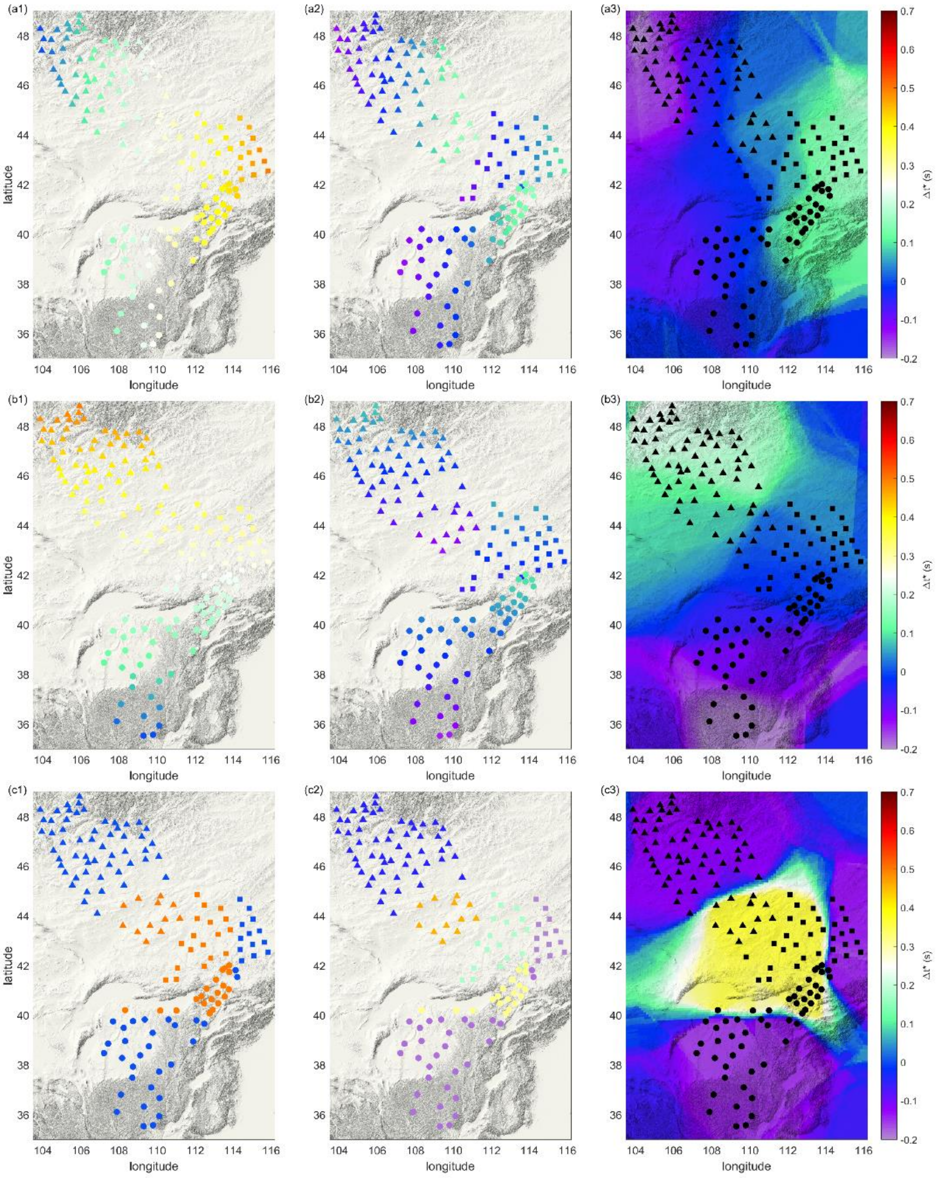

Fig 6.

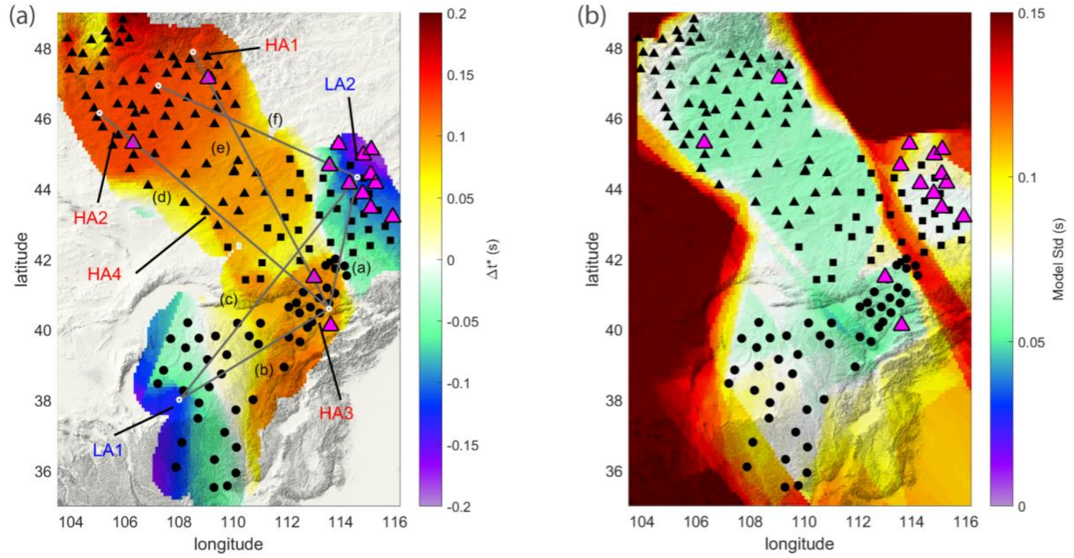

(a)
HA1
LA2
HA2
HA4
HA3
LA1
(a)
(b)
(c)
(d)
(e)
(f)
latitude
longitude
Δt* (s)
(b)
Model Std (s)

Fig 7.

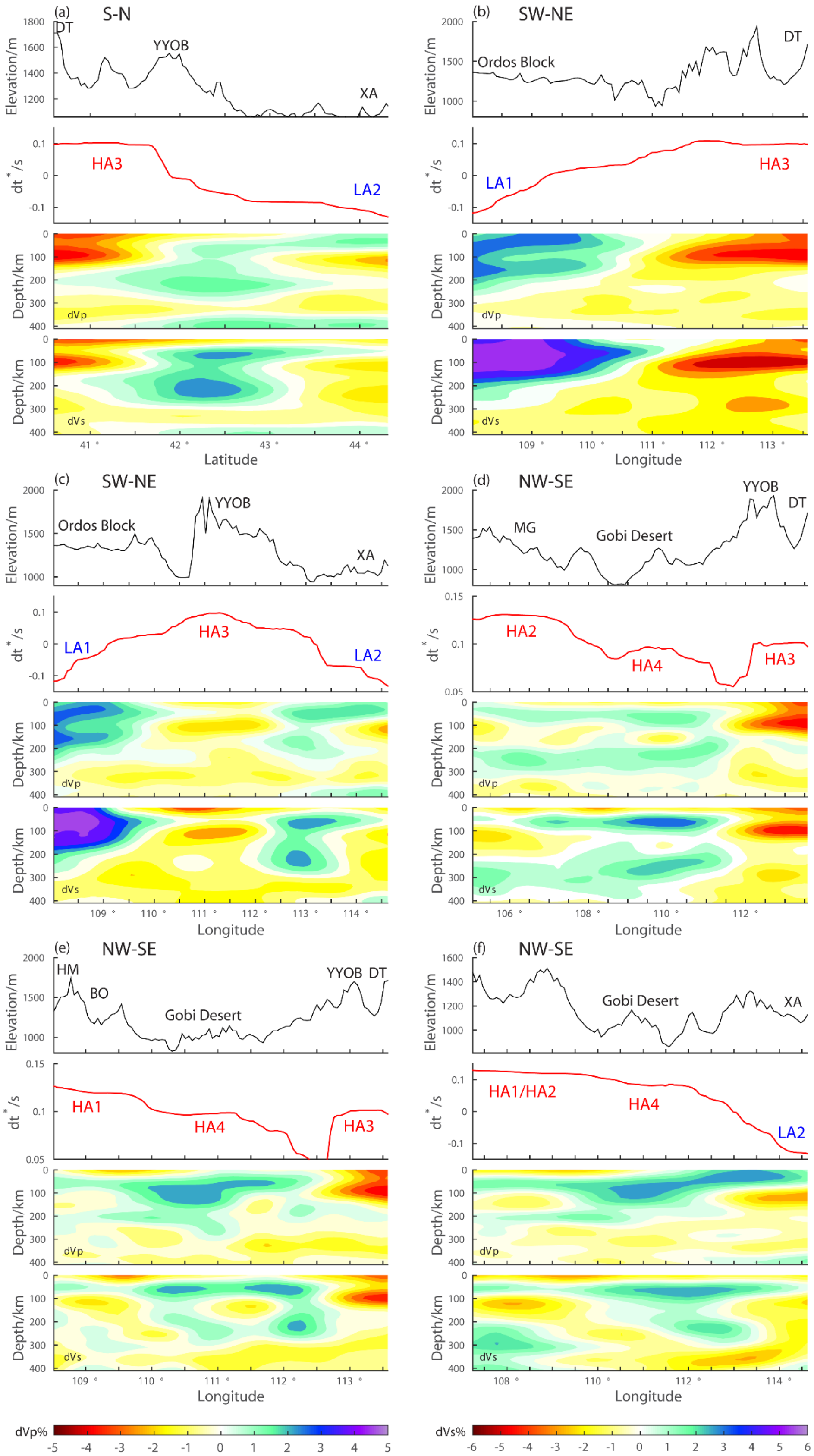

(a) S-N
DT
YYOB
XA
HA3
LA2
dVp
dVs
Latitude
(b) SW-NE
Ordos Block
DT
LA1
HA3
Longitude
(c) SW-NE
Ordos Block
YYOB
XA
LA1
HA3
LA2
Longitude
(d) NW-SE
MG
Gobi Desert
YYOB
DT
HA2
HA4
HA3
Longitude
(e) NW-SE
HM
BO
Gobi Desert
YYOB DT
HA1
HA4
HA3
Longitude
(f) NW-SE
Gobi Desert
XA
HA1/HA2
HA4
LA2
Longitude
Elevation/m
dt*/s
Depth/km
dVp%
dVs%

923 **Fig 8.**

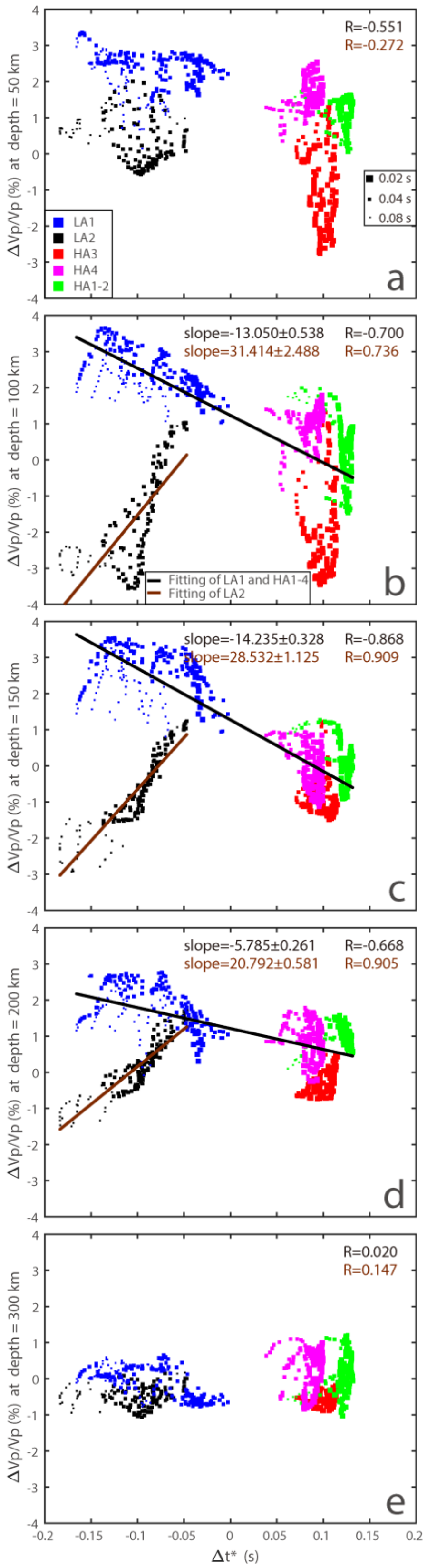

924

925

Fig 9.

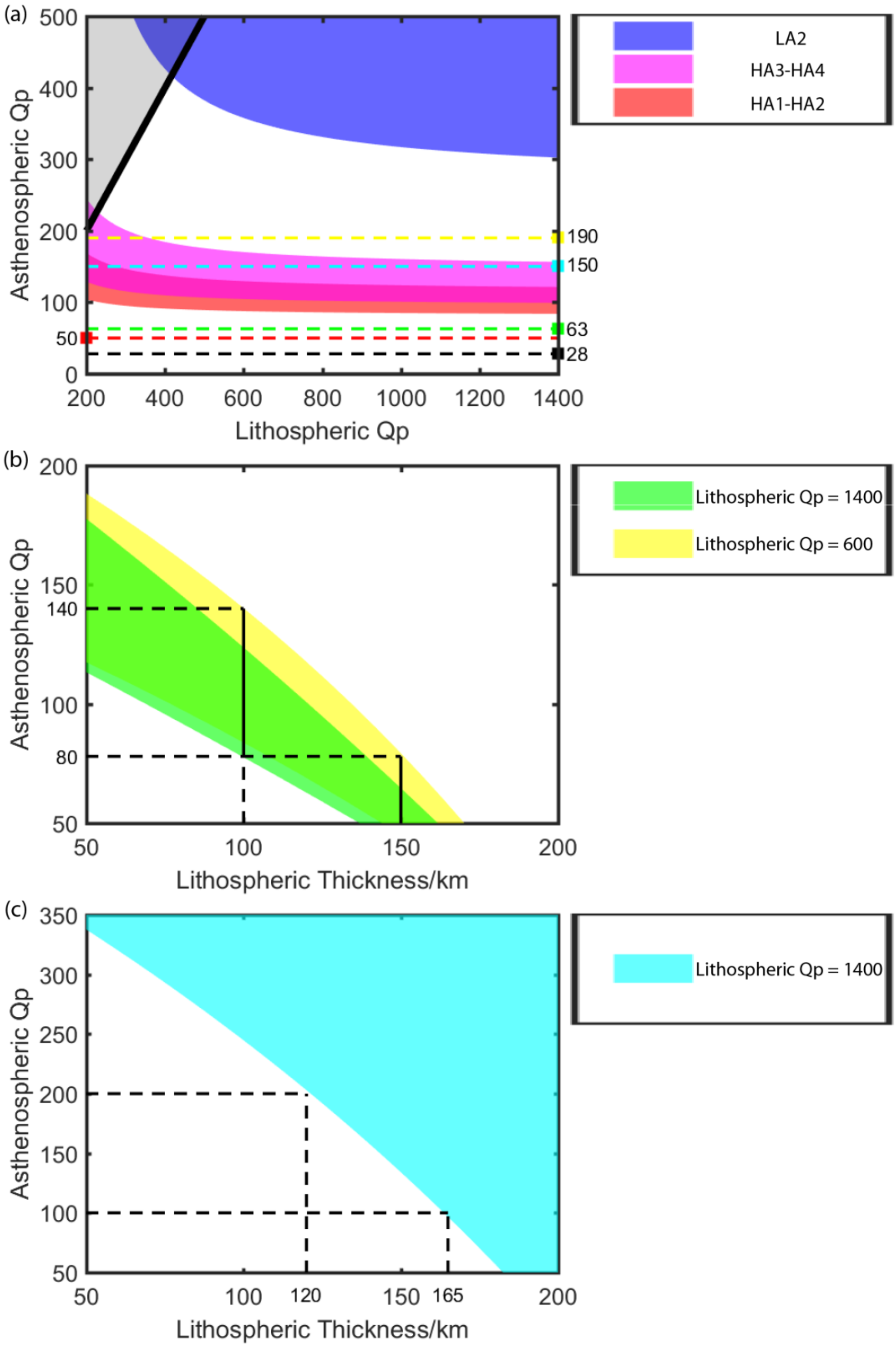

(a)
Asthenospheric Qp
Lithospheric Qp
500
400
300
200
100
50
0
200
400
600
800
1000
1200
1400
190
150
63
28
LA2
HA3-HA4
HA1-HA2
(b)
Asthenospheric Qp
Lithospheric Thickness/km
200
150
140
100
80
50
50
100
150
200
Lithospheric Qp = 1400
Lithospheric Qp = 600
(c)
Asthenospheric Qp
Lithospheric Thickness/km
350
300
250
200
150
100
50
50
100
120
150
165
200
Lithospheric Qp = 1400

929 **Fig 10.**

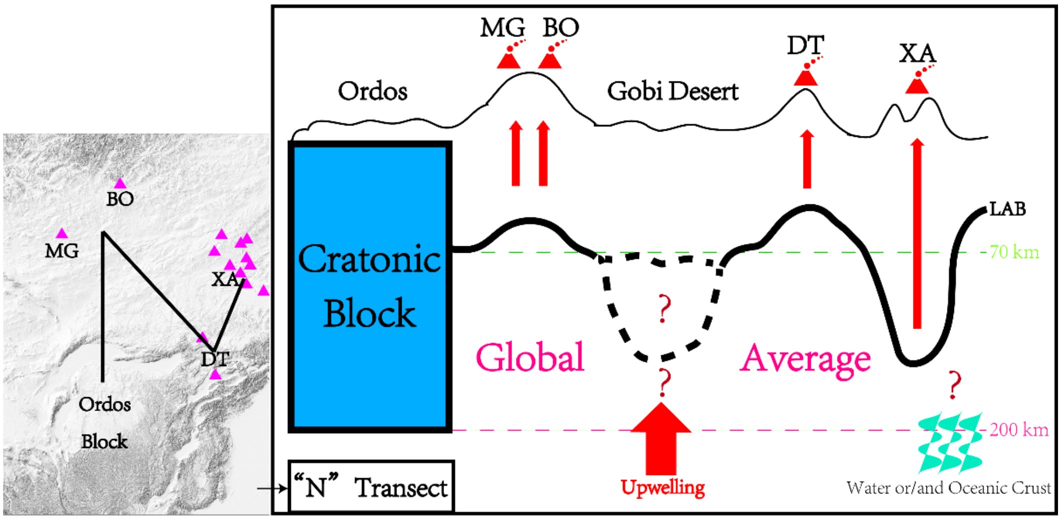

930

931